ChemComm

Chemical Communications

Accepted Manuscript

This article can be cited before page numbers have been issued, to do this please use: A. Dey, S. Akter, A. K. Thapa, J. B. Jasinski and H. Wang, *Chem. Commun.*, 2026, DOI: 10.1039/D6CC02378A.

ROYAL SOCIETY OF CHEMISTRY

rsc.li/chemcomm

ChemComm

View Article Online
DOI: 10.1039/D6CC02378A

COMMUNICATION

Synthesis Route Effects on Structure and Electrochemical Performance of Layered Oxide Cathode for Na-ion Batteries

Arnob Dey, [a] Sharmin Akter, [a] Arjun Thapa,[b] Jacek B. Jasinski, [b] and Hui Wang [a] *

Received 00th January 20xx,
Accepted 00th January 20xx

DOI: 10.1039/x0xx00000x

The synthesis routes play a critical role in determining the structural and electrochemical stability of layered oxide cathode for sodium ion batteries. In this work, using $Na_{0.67}Fe_{0.5}Mn_{0.5}O_2$ as a model layered oxide cathode, we investigated two synthesis methods, specifically, co-precipitation and solid-state reaction, to elucidate their influence on phase, morphology and electrochecmial performance. The structural and electrochemical characteriztaion reveal that the co-precipitation-derived materials exhibit superior cycling stability and higher revesible capacity compared to their solid-state counterparts. The improved performance is attributed to the formation of fine, homogeous morphology and high phase purity. These findings highlight the imporant role of synthesis in controlling particle morphology and phase purity, toward high-performance, structurally stability sodium-ion battery cathode.

1. Introduction

Layered transition-metal oxide cathodes Na_xTMO_2 (TM=Ni, Mn, Co, Fe, etc), as counterpart materials for $LiCoO_2$ used in commercial Lithium-ion batteries (LIBs), have emerged as promising cathode materials for cost-effective and large-scale sodium-ion batteries (SIBs).[1, 2] Compared with other cathode materials (e.g., phosphates, Prussian blue analogues), Na_xTMO_2 compounds offer several advantages, such as high operating voltage and specific energy density, tuneable structure and composition, etc.[3-5] Depending on the stacking sequence of oxygen layers and the coordination environment of Na^+ ions, Na_xTMO_2 cathode materials can adopt various structural types (O3- and P2- types). In O-type structures, Na^+ ions occupy octahedral sites, while they reside in prismatic sites in P-type structure. These structural configurations govern interlayer spacing and Na^+ diffusion pathways, thereby influencing their structural stability, ion diffusion, and electrochemical performance such as capacity and rate capability. [6]

Due to their use of earth abundant elements, environmental benignity, high specific capacity, Mn-based layered oxide cathodes (P2- and O3- type) are particularly attractive among various transition metal systems.[4, 7, 8] However, their cycling stability remains limited due to the complex phase transition during Na^+ ions extraction,[9] resulting in structural instability, consequent capacity fading and poor rate performance.[10, 11] To mitigate these issues, extensive efforts have focused on doping strategies (cation or anion substitution), optimization of Na content and phase ratio, interface engineering and surface coating, etc.[12-15] For instance, Hu et al. reported that Mg^{2+} incorporation activates the oxygen redox process in O3-type $NaFe_{0.5}Mn_{0.5}O_2$ cathode, achieving a high charge capacity of 207 mAh g^{-1}.[16] Qi et al. demonstrated that Li/Cu co-doping in a P2-type $Na_{0.65}Li_{0.08}Cu_{0.08}Fe_{0.24}Mn_{0.6}O_2$ cathode enhanced cycling stability (88.2% capacity retention after 500 cycles) and rate performance by reducing volume change.[17]

In addition to compositional design, the synthesis process also plays a crucial role to influence the crystalline, structural integrity and electrochemical performance of Mn/Fe-based layered oxides.[18, 19] The popular solid-state synthesis route involves high-temperature calcination (typically 800–1000 °C) of stoichiometric mixtures of sodium and transition-metal precursors in an oxygen-rich atmosphere. Besides, solution-based synthesis approaches (e.g., co-precipitation, sol–gel, and spray pyrolysis, etc) are also developed to enable finer control over crystal growth, particle size, and phase purity. The choice of synthesis method has a significant influence on the crystallographic phase composition (P2-, O3-, or mixed-structure), particle size, and defect concentration of Na-layered oxides, all of which directly affect Na^+ diffusion kinetics and structural reversibility during electrochemical cycling [20].

Developing effective and scalable synthesis strategies to Mn/Fe-based layered cathodes is crucial to optimizing their electrochemical performance in SIBs. Nevertheless, a systematic comparison between solid-state synthesis and co-precipitation synthesis routes remains rarely reported. Here, $Na_{0.67}Fe_{0.5}Mn_{0.5}O_2$ is employed as a model system due to its earth-abundant composition, balanced Mn/Fe redox activity, and stable P2-type structure. The carbonate co-precipitation and solid-state synthesis routes are comparatively investigated. Detailed structural and morphological characterizations are

[a] Mechanical Engineering Department, University of Louisville, Louisville, KY, 40292
[b] Conn Center for Renewable Energy Research, University of Louisville, Louisville, KY, 40292
* Corresponding author: hui.wang.1@louisville.edu
Supplementary Information available: [details of any supplementary information available should be included here]. See DOI: 10.1039/x0xx00000x

performed to elucidate their distinct reaction mechanisms and their impact on phase formation, crystallinity and electrochemical cycling performance.

2. Results and Discussion

Figure 1 illustrates the schemes for co-precipitation and solid-state synthesis routes. In the co-precipitation synthesis (**Figure 1a**), two precursor solutions (aqueous 1M $FeSO_4$ and 1M $MnSO_4$) were mixed in a 1:1 molar ratio under magnetic stirring, as well as CO_2 gas flow to facilitate the precipitation of $Fe_{0.5}Mn_{0.5}CO_3$. The resulting precipitate was filtered, washed and dried, followed by two-step heating treatment (450°C, 850°C) process with Na_2CO_3 in a stoichiometric ratio of $Na_{0.67}Fe_{0.5}Mn_{0.5}O_2$ (CP-NFMO-850). For the solid-state synthesis (**Figure 1b**), stoichiometric amounts of Na_2CO_3, Fe_2O_3, and Mn_2O_3 precursors were thoroughly mixed, and ball milled for 2 hours. The resulting mixture was calcinated through two-step heat treatment (450°C, 850°C), then cooled down to room temperature to obtain $Na_{0.67}Fe_{0.5}Mn_{0.5}O_2$ (SS-NFMO-850).

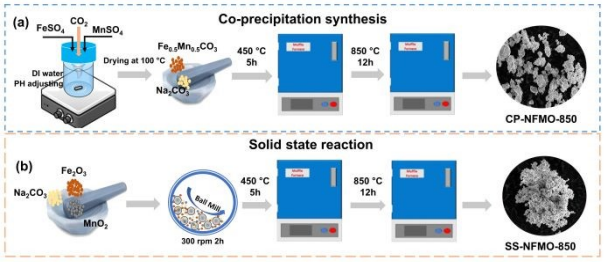

Figure 1. Scheme of two synthesis methods: (a) co-precipitation, (b) solid-state.

To investigate the synthesis pathways of the two approaches, intermediate products collected at different stages were examined by X-ray diffraction (XRD) and scanning electron microscopy (SEM) to characterize the structural and morphological evolution. **Figure 2a** presents the XRD patterns of the co-precipitation derived samples: $Fe_{0.5}Mn_{0.5}CO_3$ (CP-FMO), the product after sodiation at 450 °C (CP-NFMO-450), and after 850 °C sodiation (CP-NFMO-450), respectively. When synthesized at room temperature and pH<7, the co-precipitated $Fe_{0.5}Mn_{0.5}CO_3$ (CP-FMO) exhibits characteristic diffraction peaks at 2θ=32.1°, 42.2°, and 52.5° indexed to a rhombohedral carbonate phase.[21] Upon using Na_2CO_3 as the sodium source and heating treatment at 450 °C, the carbonate peaks disappear, while a new diffraction peak appears at 2θ=15.7°, indicating the formation of an intermediate layered oxide phase. Notably, this phase has previously been reported to form above 550 °C when NaOH is used as the sodium source,[22] suggesting that the carbonate-assisted reaction pathway facilitates phase formation. After calcination at 850 °C, the CP-NFMO-850 sample exhibits strong diffraction peaks at 2θ=15.73°, 35.45°, 38.99°, 48.47°, corresponding to the (002), (100), (102), (103) planes of the P2-type layered structure (space group: P63/mmc).

Figure 2b shows the XRD patterns of the solid-state-derived samples: ball-milled precursors (BM-NFMO), heat-treated at 450 °C (SS-NFMO-450), and calcinated at 850 °C (SS-NFMO-850). The BM-NFMO displays diffraction peaks corresponding to individual precursors: MnO_2 (2θ=28.7°,37.2°), Fe_2O_3 (2θ=33°, 35°, 37.2°), Na_2CO_3 (2θ=30°, 35°, 38°), and mixed phase $FeMn_2O_4$(2θ=56.5°, 57.4°, 63°). After heating at 450°C, the diffraction patterns remain dominated by precursors, excepting a minor peak emerging at 2θ =15.7°, which indicate the initial solid-state sodiation reaction. With increasing heat-treatment temperature to 850 °C, the precursor peaks completely disappear, and new diffraction patterns show similar peaks with CP-NFMO-850 sample. XRD Rietveld refinement results for synthesized CP-NFMO-850 and SS-NFMO-850 samples are displayed in **Figure 2 c,d** and Table S1. Both samples predominately crystallize in a P2-type layered structure, with interlayer spacing of ~5.630 Å. No O3-type phase observed for NFMO-850 for either synthesis method, as evidenced by the absence of the diffraction peak at 2θ=16-17° for (003) plane.

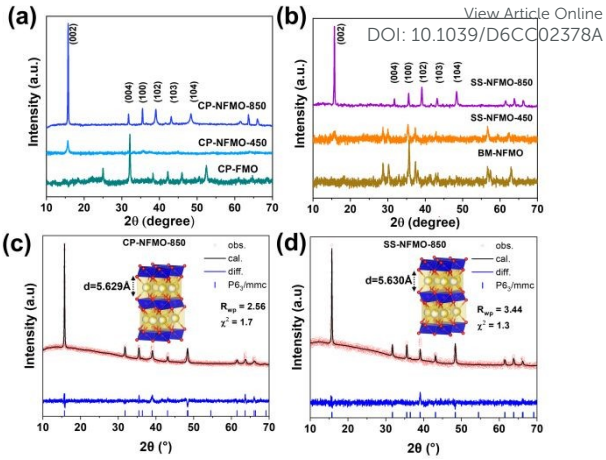

Figure 2. XRD patterns of intermediate products from (a) co-precipitation method, (b) solid-state reaction method; Rietveld refinement results for (c) CP-NFMO-850, and (d) SS-NFMO-850 samples.

The morphological evolution during the co-precipitation process is shown in **Figure 3a-c**. The as-prepared CP-FMO precursor exhibits spherical particles. After sodiation at 450 °C and calcination at 850 °C, the dispersed spherical morphology is retained with a uniform particle size. For the solid-state synthesis route (**Figure 3d-f**), ball-milled precursors consist of large, irregular aggregates formed by clustering of smaller secondary particles. This morphology remains largely unchanged after heating at 450 °C and calcination at 850 °C, consistent with typical morphologies reported for solid-state synthesized layered oxides.[23] Particle size distribution analysis based on SEM image (**Figure S1**) confirms that the CP method produces a narrower size distribution with particle size of 3-8 μm, compared to broader range of 4-40 μm observed for solid-state synthesis. Finer particle size is considered to be beneficial for the electrochemical performance.[24]

High resolution transmission electron microscopy (HRTEM) was further employed to examine the microstructure of the CP-NFMO-850 (**Figure 3g,h**) and SS-NFMO-850 samples (**Figure 3i,j**). The TEM observations are consistent with the SEM analysis, revealing that the CP-derived NFMO sample exhibits smaller and more uniform secondary particles compared to the SS-derived NFMO counterpart. Clear lattice fringes are

observed in the high magnification HRTEM images (Figure 3h, j), with an interlayer space of ~5.60 Å, corresponding to the (002) planes of the layered structure. The corresponding FFT patterns (insets), together with the in-plane TEM images and their FFT patterns (Figure S2) further confirm high crystallinity and well-ordered P2-type structure. Additional TEM images from different regions, along with EDS-based elemental mapping are presented in Figure S3 and S4. The CP-derived NFMO sample shows a uniform elemental distributions of Na, Fe, Mn, O, consistent with previous report on Mn-rich layered oxide cathode via co-precipitation method.[25] In contrast, the SS-NFMO-850 sample displays relatively inhomogeneous elemental distributions. Specifically, Na and O are more accumulated on the edge rather than centre area. This observation is also further supported by the HAADF spectrum for SS-NFMO-850 sample (Figure S5), whereas the atomic fraction of Na (7.07%) is much less than that of Mn (20.91%) and Fe (21.83%). The Na deficiency observation is related to Na-loss during high temperature calculation for solid-state synthesis method.[26] In comparison, the CP-derived sample exhibits higher Na contents (12-15%, Figure S6).

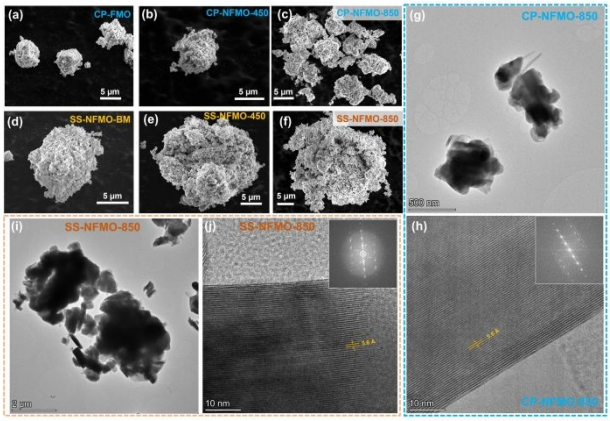

Figure 3. SEM images for co-precipitated synthesis: (a) CP-FMO, (b) CP-NFMO-450; (c) CP-NFMO-850; SEM images for solid-state synthesis: (d) SS-BM; (e) SS-NFMO-450; (f) SS-NFMO-850; HRTEM and EDX mapping for (g) CP-NFMO-850, and (h) SS-NFMO-850.

Both CP-NFMO-850 and SS-NFMO-850 samples were employed to assemble half-cells with Na metal as anode using liquid electrolyte (1M $NaPF_6$ in EC/DMC in 1:2 vol ratio with 5 vol% FEC). When cycling between voltage window of 1.5-4.2 V, **Figure 4a** presents the galvanostatic charge-discharge profile for CP-NFMO-850 sample. The cell delivers an initial specific discharge capacity of 135 mAh g^{-1} at 1C (1C=140 $mAhg^{-1}$). Then the specific capacity slightly drops to 128 mAh g^{-1} for 20th cycle, and to 100 $mAhg^{-1}$ for 50th cycle, indicating relatively stable cycling. In contrast, the cell with SS-NFMO-850 cathode not only exhibits a lower initial specific capacity (127 mAh g^{-1} at 1C) but also a rapid capacity fading (**Figure 4b**). Notably, the capacity drops below 80 mAh g^{-1} after 20 cycles. Similar rapid degradation has been reported in solid-state synthesised NFMO under various calcination temperatures (850-1000) at 0.1C.[23] This comparison reveals that the CP-NFMO cathode shows superior structural and electrochemical stability compared to that of SS-NFMO. **Table S2** summarize the electrochemical performance between the present CP-NFMO and previously reported NFMO cathode.

The differential capacity (dQ/dV) plots further elucidate the capacity-fading mechanism in these two samples (**Figure S7**). There are three pair of redox peaks observed, including the Mn^{3+}/Mn^{4+} redox region at 2.0-2.7V, Fe^{3+}/Fe^{4+} redox region at 3.2-3.8V, and the peaks beyond 4.0V from oxygen redox. [15] Upon cycling, the CP-NFMO-850 cathode exhibits obvious redox peaks (blue curves), and narrower polarization from 2nd to 20th cycle than that of SS-NFMO-850 sample (pink curves). Detailed comparison for 2nd, 3rd, 5th, 10th, and 20th cycles (Figure S8) reveal this trend more obviously, whereas minor polarization increases for CP-NFMO cathode but rapidly diminishing peak for SS-NFMO sample. These results reveal that co-precipitation method effectively enhances redox reversibility compared to the conventional solid-sate synthesis for NFMO cathode.

To further investigate the Na^+ ion diffusion kinetics, the galvanostatic intermittent titration technique (GITT) was performed. As shown in **Figure 4c**, higher voltage plateaus are observed for the CP-NFMO electrode in both charge and discharge cycles within the Mn^{3+}/Mn^{4+} and Fe^{3+}/Fe^{4+} redox regions, which is beneficial to achieve higher energy density.[27] Furthermore, the average Na^+ diffusion coefficient for the CP-NFMO during the discharge process is 1.84×10^{-9} cm^2s^{-1} (Figure S9), higher than that of the SS-NFMO (1.16×10^{-9} cm^2s^{-1}). This comparison indicates the faster Na^+ diffusion in CP-NFMO cathode than that in SS-NFMO. The cycling stability of CP-NFMO-850 cathode was demonstrated up to 100 cycles at 1C (**Figure 4d**). In contrast, the SS-NFMO cathode shows poor capacity remain after 100 cycles (Figure S10). Moreover, it also exhibits worse rate performance than CF-NFMO cathode (Figure S11). The post-cycling analysis was performed to characterize the crystal structures of both cathodes (CP-NFMO and SS-NFMO) after charge/discharge for 100 cycles. The XRD results (Figure S12) reveal that new diffraction peak at 2θ=18.02° emerges for the SS-NFMO sample, which suggests the phase transition from P2 to spinel phase upon repeated cycling. In contrast, the CP-NFMO cathode displays almost identical diffraction patterns with the pristine sample, indicating its structural stability during electrochemical cycling.

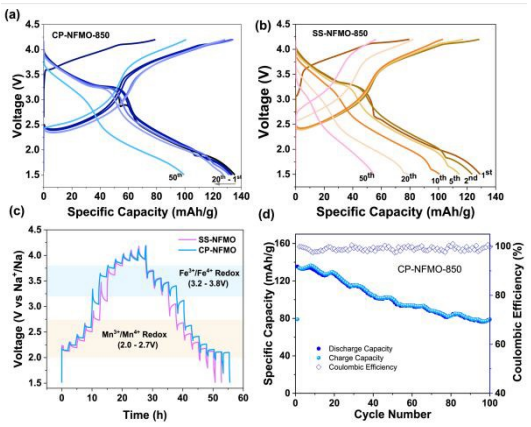

Figure 4. Charge/discharge profiles of (a) CP-NFMO, and (b) SS-NFMO; (c) dB/dV plots, (d) electrochemical cycling performance of CP-NFMO.

3. Conclusion

In summary, electrochemical and structural analyses confirm that the co-precipitation synthesis route yields superior $Na_{0.67}Fe_{0.5}Mn_{0.5}O_2$ cathodes compared to solid-state synthesis method. Although both synthesis approach generates P2-type crystal structure, CP-derived sample exhibits finer particle size and homogenous compositions as well as less Na loss after calcination, contributing to fast Na+ diffusion. For the half cells, the co-precipitation-derived sample delivers higher reversible capacity (138 mAh g^{-1} initial discharge capacity at 1C), slower capacity fading, supported by stable voltage profiles, reversible redox peaks and higher capacity retention. The post-cycling analysis reveals that CP-NFMO sample exhibits higher structural stability upon repeated cycling. Overall, the co-precipitation approach enables better control of morphology and phase formation, resulting in improved Na^+ diffusion kinetics and superior electrochemical performance for sodium-ion battery.

Data availability

The data supporting this article have been included as part of the Supplementary Information, including Experimental section, SEM images, HRTEM images, TEM/STEM images, HAADF-STEM images and EDS spectrum, dQ/dV curves, Diffusion coefficient, and electrochemical cycling performance.

Conflicts of interest

There are no conflicts to declare.

Acknowledgements

The authors thank for the funding support from U.S. Department of Energy, Office of Science, Basic Energy Sciences, under Award # DE-SC0024131.

References

1. Y. Zhang, G.-Q. Liu, Q. Sun, D. Qiao, J. Chen, L. Wen and M. Zhao, *Journal of Energy Storage*, 2024, **102**, 114279.
2. X. Liang, X. Song, H. H. Sun, H. Kim, M.-C. Kim and Y.-K. Sun, *Nature Communications*, 2025, **16**.
3. V. P. Mhaske, S. Jilkar and M. D. Yadav, *Energy & Fuels*, 2023, **37**, 16221-16244.
4. B. Peng, Z. Zhou, J. Shi, X. Huang, Y. Li and L. Ma, *Advanced Functional Materials*, 2024, **34**.
5. J. Liu, N. Zhang, H. Shi, Z. He, Z. Zhang, D. V. Anishchenko, E. V. Alekseeva, R. Li, P. Yang, O. V. Levin, D. Wang, H. Liu, S. Dou and B. Wang, *Chemical Engineering Journal*, 2025, **521**, 167111.
6. C. Zhao, Q. Wang, Z. Yao, J. Wang, B. Sánchez-Lengeling, F. Ding, X. Qi, Y. Lu, X. Bai, B. Li, H. Li, A. Aspuru-Guzik, X. Huang, C. Delmas, M. Wagemaker, L. Chen and Y.-S. Hu, *Science*, 2020, **370**, 708-711.
7. S. Chu, S. Guo and H. Zhou, *Chemical Society Reviews*, 2021, **50**, 13189-13235.
8. T. Chen, B. Ouyang, X. Fan, W. Zhou, W. Liu and K. Liu, *Carbon Energy*, 2022, **4**, 170-199. DOI: 10.1039/D6CC02378A
9. Q. Wang, S. Mariyappan, J. Vergnet, A. M. Abakumov, G. Rousse, F. Rabuel, M. Chakir and J.-M. Tarascon, *Advanced Energy Materials*, 2019, **9**, 1901785.
10. G. Zhang, J. Li, Y. Fan, Y. Liu, P. Zhang, X. Shi, J. Ma, R. Zhang and Y. Huang, *Energy Storage Materials*, 2022, **51**, 559-567.
11. R. Liu, W. Huang, J. Liu, Y. Li, J. Wang, Q. Liu, L. Ma, G. Kwon, S. N. Ehrlich, Y. Wu, T. Liu, K. Amine and H. Li, *Advanced Materials*, 2024, **36**.
12. W. Huang, T. Liu, L. Yu, J. Wang, T. Zhou, J. Liu, T. Li, R. Amine, X. Xiao, M. Ge, L. Ma, S. N. Ehrlich, M. V. Holt, J. Wen and K. Amine, *Science*, 2024, **384**, 912-919.
13. E. Boivin, R. A. House, J. J. Marie and P. G. Bruce, *Advanced Energy Materials*, 2022, **12**, 2200702.
14. Y. Yang, Z. Wang, C. Du, B. Wang, X. Li, S. Wu, X. Li, X. Zhang, X. Wang, Y. Niu, F. Ding, X. Rong, Y. Lu, N. Zhang, J. Xu, R. Xiao, Q. Zhang, X. Wang, W. Yin, J. Zhao, L. Chen, J. Huang and Y.-S. Hu, *Science*, 2024, **385**, 744-752.
15. D. Wang, F. Zou, W. Lin, X. Zhang, X. Zhang, X. Qi, S. Xu, H. Mao, D. Xiao, S. Lu, B. Guo, Y. S. Hu and Y. Lyu, *Advanced Science*, 2025, DOI: 10.1002/advs.202501852.
16. Y. Niu, Z. Hu, B. Zhang, D. Xiao, H. Mao, L. Zhou, F. Ding, Y. Liu, Y. Yang, J. Xu, W. Yin, N. Zhang, Z. Li, X. Yu, H. Hu, Y. Lu, X. Rong, J. Li and Y. S. Hu, *Advanced Energy Materials*, 2023, **13**.
17. R. Qi, M. Chu, W. Zhao, Z. Chen, L. Liao, S. Zheng, X. Chen, L. Xie, T. Liu, Y. Ren, L. Jin, K. Amine, F. Pan and Y. Xiao, *Nano Energy*, 2021, **88**, 106206.
18. C. Hakim, N. Sabi and I. Saadoune, *Journal of Energy Chemistry*, 2021, **61**, 47-60.
19. H. Xu, Q. Yan, W. Yao, C.-S. Lee and Y. Tang, *Small Structures*, 2022, **3**, 2100217.
20. J. Lamb and A. Manthiram, *Chemistry of Materials*, 2020, **32**, 8431-8441.
21. T. Deng, X. Fan, J. Chen, L. Chen, C. Luo, X. Zhou, J. Yang, S. Zheng and C. Wang, *Advanced Functional Materials*, 2018, **28**, 1800219.
22. A. T. Promi, J. Yao, D. Xia, C. Connor, A. U. Olayiwola, J. Bai, C. Sun, D. Nordlund, K. Zhao and F. Lin, *Journal of Materials Chemistry A*, 2025, **13**, 17063-17074.
23. L. Qian, R. Huang, H. Zhang, S. Yan and S. Luo, *ACS Applied Energy Materials*, 2024, **7**, 8136-8146.
24. V. K. Kumar, S. Ghosh, S. Biswas and S. K. Martha, *Journal of The Electrochemical Society*, 2021, **168**, 030512.
25. N. Zhang, X. Fan, Y. Tong, M. Wang, H. Ding, J. Zhou, X. Li, D. Zhao and S. Li, *Ionics*, 2025, **31**, 1483-1497.
26. P.-F. Wang, Y. You, Y.-X. Yin and Y.-G. Guo, *Advanced Energy Materials*, 2018, **8**, 1701912.
27. J. Jiao, E. Zhao, W. Yin, J. Che, Y. Cheng, Z. Xia, X. Xiao and X. Zhang, *Small*, 2024, **20**.

View Article Online
DOI: 10.1039/D6CC02378A

Synthesis Route Effects on Structure and Electrochemical Performance of Layered Oxide Cathode for Na-ion Batteries

Arnob Dey, Sharmin Akter, Jacek Jasinski, Arjun Thapa, and Hui Wang

The data supporting this article have been included as part of the Supplementary Information, including Experimental section, SEM images, HRTEM images, TEM/STEM images, HAADF-STEM images and EDS spectrum, dQ/dV curves, Diffusion coefficient, and electrochemical cycling performance.